

# Direct Visualization of the Reversible $O^{2-}/O^-$ Redox Process in Li-Rich Cathode Materials

Xiang Li, Yu Qiao, Shaohua Guo,\* Zhenming Xu, Hong Zhu, Xiaoyu Zhang, Yang Yuan, Ping He,\* Masayoshi Ishida, and Haoshen Zhou\*

Conventional cathodes of Li-ion batteries mainly operate through an insertion–extraction process involving transition metal redox. These cathodes will not be able to meet the increasing requirements until lithium-rich layered oxides emerge with beyond-capacity performance. Nevertheless, in-depth understanding of the evolution of crystal and excess capacity delivered by Li-rich layered oxides is insufficient. Herein, various in situ technologies such as X-ray diffraction and Raman spectroscopy are employed for a typical material  $Li_{1.2}Ni_{0.2}Mn_{0.6}O_2$ , directly visualizing  $O^-–O^-$  (peroxo oxygen dimers) bonding mostly along the *c*-axis and demonstrating the reversible  $O^{2-}/O^-$  redox process. Additionally, the formation of the peroxo  $O–O$  bond is calculated via density functional theory, and the corresponding  $O–O$  bond length of  $\approx 1.3$  Å matches well with the in situ Raman results. These findings enrich the oxygen chemistry in layered oxides and open opportunities to design high-performance positive electrodes for lithium-ion batteries.


The applications of lithium-ion batteries (LIBs) like mobile devices are familiar in our daily lives.<sup>[1]</sup> However, the energy density of nowadays LIBs is still unsatisfying toward our increasing requirements.<sup>[2,3]</sup> The most common positive electrodes, such as  $LiCoO_2$ ,  $LiFePO_4$ , and  $LiMn_2O_4$ , are still limited to the unsatisfied capacity, hindering the development of LIBs.<sup>[4]</sup> To allay the gap between supply and demand, we should

X. Li, Prof. S. H. Guo, Dr. X. Y. Zhang, Y. Yuan, Prof. P. He, Prof. H. S. Zhou  
Center of Energy Storage Materials and Technology  
College of Engineering and Applied Sciences  
National Laboratory of Solid State Microstructures, and Collaborative  
Innovation Center of Advanced Microstructure  
Nanjing University  
Nanjing 210093, China  
E-mail: shguo@nju.edu.cn; pinghe@nju.edu.cn; hszhou@nju.edu.cn

X. Li, Y. Qiao, Prof. M. Ishida  
Graduate School of System and Information Engineering  
University of Tsukuba  
Tennoudai 1-1-1, Tsukuba 305-8573, Japan

X. Li, Prof. S. H. Guo, Prof. H. S. Zhou  
Energy Technology Research Institute  
National Institute of Advanced Industrial Science and Technology (AIST)  
Umezono 1-1-1, Tsukuba 305-8568, Japan

Z. Xu, Prof. H. Zhu  
University of Michigan-Shanghai Jiao Tong University Joint Institute  
Shanghai Jiao Tong University  
Shanghai 200240, China

 The ORCID identification number(s) for the author(s) of this article can be found under <https://doi.org/10.1002/adma.201705197>.

DOI: 10.1002/adma.201705197

settle the capacity issue. Therefore, aiming at improving the battery performance, a lot of efforts have been made in searching for better electrode materials with high capacity and good cyclic ability.<sup>[5]</sup>

Recently, lithium-rich layered oxides like  $Li_{1.2}Ni_{0.166}Co_{0.067}Mn_{0.567}O_2$  with higher capacities than  $250\text{ mA h g}^{-1}$  were reported.<sup>[6]</sup> These Li-rich materials can deliver excess capacity beyond the theoretical capacity based on cationic redox process, having received worldwide attention. The compounds  $(1-x)LiNi_{0.5}Mn_{0.5}O_2 \cdot xLi_2MnO_3$ , which can be also written as  $Li[Li_{(1-2x)/3}Ni_xMn_{(2-x)/3}O_2]$ , are well known.<sup>[7,8]</sup> However, the mechanism based on cationic redox process is unable to explain the anomalous capacities exhibited by Li-rich materials. Thus,

another new process, oxygen activation has been proposed to account for the phenomenon. Luo et al. pointed out that localized electron holes are formed on oxygen ions with the configuration surrounding by  $Mn^{4+}$  and  $Li^+$  in  $Li_{1.2}[Ni_{0.13}Co_{0.13}Mn_{0.54}]O_2$ .<sup>[9]</sup> Seo et al. depicted that oxygens are easily oxidized due to the  $Li–O–Li$  configuration.<sup>[10]</sup> Sathiyaraj et al. observed the peroxo-like species formed reversible in  $Li_2Ru_{1-y}Sn_yO_3$ .<sup>[11]</sup> However, all above-mentioned results are lacking in direct especially in situ evidence for deep insight into the microstructure evolution of Li-rich layered oxides. McCalla et al. visualized the  $O–O$  dimers via transmission electron microscopy (TEM) and neutron powder diffraction by using  $Li_2IrO_3$  as a model compound and determined the possible limits on the value of *n* for peroxo-like  $O_2^{n-}$  dimers (the lower bound  $n = 3$  and the upper  $n = 3.3$ ), leading to a further understanding of anionic redox process.<sup>[12]</sup> Here, we focus on the representative material  $Li_{1.2}Ni_{0.2}Mn_{0.6}O_2$  and investigate its charge–discharge processes during initial cycles by in situ X-ray diffraction (XRD) and in situ Raman spectroscopy. We demonstrate the structural change by the continuous shift of *c*-parameter and the direct evidence of peroxo  $O–O$  bond formation and extinction ( $O_2^{2-}$  dimers). What is more, the well reversible formation/extinction of the dimers can be clearly observed in subsequent cycles, accompanied with synchronous structural change. Moreover, we can speculate that the peroxo  $O–O$  bond is along the *c*-axis by combining the variation trend of *c* lattice and peroxo  $O–O$  bond distance. Our findings provide a direct and new evidence for the reversible anionic redox chemistry in Li-rich cathode materials and a guideline toward designing the next generation of cathode

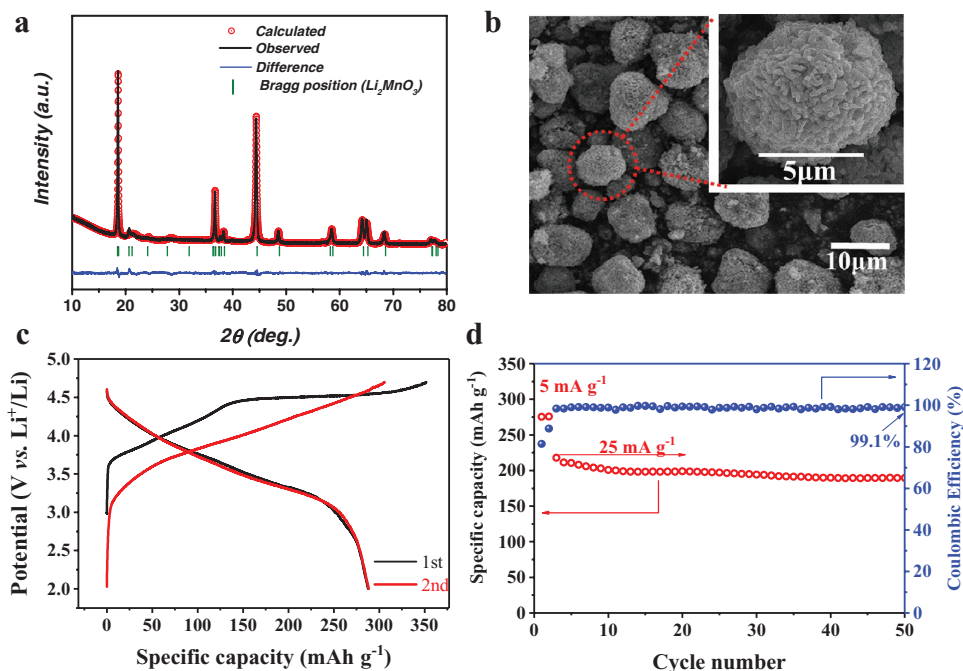


**Figure 1.** XRD, SEM, and electrochemical characterizations of  $\text{Li}_{1.2}\text{Ni}_{0.2}\text{Mn}_{0.6}\text{O}_2$ . a) XRD patterns of  $\text{Li}_{1.2}\text{Ni}_{0.2}\text{Mn}_{0.6}\text{O}_2$  and Rietveld refinement. b) SEM images of  $\text{Li}_{1.2}\text{Ni}_{0.2}\text{Mn}_{0.6}\text{O}_2$ . The inset shows a zoom-in image of the particle marked by the red dotted line. c) Typical charge–discharge profiles between 2.0 and 4.7 V at  $5 \text{ mA g}^{-1}$ . d) The cycling performance with coulombic efficiency at  $5 \text{ mA g}^{-1}$  (first two cycles) and  $25 \text{ mA g}^{-1}$  (subsequent cycles).

materials with both cationic and anionic reversible redox process which can deliver substantially high energy density.

The compound was characterized by powder XRD and scanning electron microscopy (SEM) in **Figure 1a,b**.  $\text{Li}_{1.2}\text{Ni}_{0.2}\text{Mn}_{0.6}\text{O}_2$  is derived from  $\text{Li}_2\text{MnO}_3$  by using  $\text{Ni}^{2+}$  to replace partial  $\text{Li}^+$  and  $\text{Mn}^{4+}$  in transition metal (TM) layers. The XRD pattern indicates that most of the diffraction lines can be well indexed to a monoclinic  $\text{Li}_2\text{MnO}_3$ -like structure with space group  $C2/m$ .<sup>[13]</sup> Rietveld refinements of the XRD pattern obtained by the General Structure Analysis System (GSAS) + EXPGUI suite<sup>[14]</sup> successfully give reasonably low  $\chi^2$  (2.72) value based on  $\text{Li}_2\text{MnO}_3$  model. The calculated XRD patterns have a good match with experimental data. The detailed refinement results are shown in Table S17 in the Supporting Information. SEM images in **Figure 1b** reveal that spheroidal particles with a diameter of around  $8 \mu\text{m}$  are secondary particles formed from primary nanocrystals. The morphology of the particles is inherited from their hydroxide precursors (**Figure S1**, Supporting Information).

The electrochemical tests of as-prepared cathode were performed galvanostatically within the potential window (vs  $\text{Li}/\text{Li}^+$ ) of 2.0–4.7 V using  $5 \text{ mA g}^{-1}$ . **Figure 1c** shows the results during the first two cycles and corresponding  $dQ/dV$  curves can be seen in **Figure S2** in the Supporting Information. During the first charging process, the peaks located at  $\approx 3.75$  and 4.2 V are ascribed to the separate oxidation of nickel. The slope and plateau in initial charging process relate to the different  $\text{Li}^+$  extraction processes. It is easy to see the capacity of first charging is  $350 \text{ mA h g}^{-1}$ , indicating there are more than 1.1  $\text{Li}^+$  removed from the structure. It is worth noting that there are only 0.4  $\text{Li}^+$  can be removed when  $\text{Ni}^{2+}$  is totally oxidized to  $\text{Ni}^{4+}$ , corresponding  $\approx 130 \text{ mA h g}^{-1}$  at this point, far less than  $350$ .<sup>[3,8,15]</sup> The capacity of first discharging is  $\approx 287 \text{ mA h g}^{-1}$ , indicating

that there are about 0.9  $\text{Li}^+$  reinserted into the structure, leading to about 0.2  $\text{Li}^+$  loss. **Figure 1d** presents the cycling performance and coulombic efficiency. The capacity retention of the cathode at  $25 \text{ mA g}^{-1}$  after 50 cycles is 90.90% with limited capacity decay. If we focus on cations in this composition, capacity will only come from Ni-based redox process because of electrochemical inertness of  $\text{Mn}^{4+}$ .<sup>[4]</sup> As mentioned above, it is available to understand the relationship between the excess capacity and the evolution of the structure.

To unveil the lithiation–delithiation mechanism in  $\text{Li}_{1.2}\text{Ni}_{0.2}\text{Mn}_{0.6}\text{O}_2$  during cycling processes, in situ XRD was performed for the initial two cycles, displayed in **Figure 2** and **Figure S4** in the Supporting Information. The XRD pattern of cathode material assembled in the in situ cell before test is shown in **Figure S3** in the Supporting Information. For the reason of structural similarity between  $\text{Li}_2\text{MnO}_3$  and  $\text{LiNi}_{0.5}\text{Mn}_{0.5}\text{O}_2$ , in situ XRD patterns can be fitted to hexagonal unit cell for convenience.<sup>[16]</sup> As it can be seen, the peak position, such as (003) and (104), changes regularly with the process of charging and discharging, representing reversible Li-ion insertion–extraction during the test. (003) peak directly reflects the evolution of  $c$  lattice parameter of the compound. Therefore, it can be used for further understanding of the phase transformation mechanism in the system. As seen in **Figure 2**, at the beginning of the first charging, (003) peak shifts to the left continuously then gradually shifts back to the high angle region till the end of charging. The electrochemical record shows the turning point of (003) shifting is around 4.5 V. It means  $c$  lattice value increases at first until the voltage reaches to 4.5 V, followed by a sequential decrease. During discharging, reversed shift compared to the charging process is obvious. The evolution of (003) peak shifting within the first two cycles can

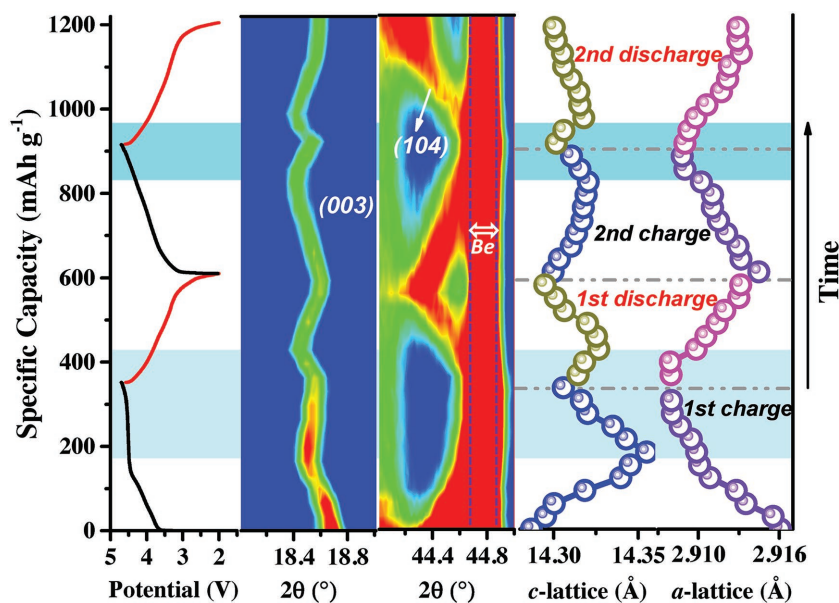


**Figure 2.** Color-coded images of the peak (003) and (104), refined  $c$ -lattice, and  $a$ -lattice parameters during initial two cycles. The range of intensity distribution plots with reference color bar is from 3000 to 5000.

be seen clearly in color graph in Figure 2. More importantly, this tendency of (003) shifts during the second cycle is similar to the first cycle.

The Rietveld refinement of the  $a$  and  $c$  lattice parameters for the structure together with corresponding unit cell volume changing during the first two cycles are displayed in Figure 2 and Figure S5 in the Supporting Information. Figure 2 discloses the  $a$ -lattice parameter continuously decrease whereas  $c$ -lattice parameter increases at the beginning and then decreases during the charge steps. At the beginning, the reduced ionic

radii in TM layers may be the reason why  $a$ -parameter decreases.<sup>[4]</sup> The extraction of  $\text{Li}^+$  from the Li-layers is accompanied by the increasing electrostatic repulsion between oxygen slabs, making an extendibility of unit cell along  $c$ -axis, corresponding to the shift of (003) to lower angles.<sup>[17]</sup> And then, the  $c$ -parameter and  $a$ -parameter change smoothly, indicating that some different reactions appear in this region. And during this region,  $\text{Li}^+$  begins to extract from the TM slabs, leading the inverse changes of unit cell and shifting (003) peak to higher reflection angles. The variation is consistent with the previous work.<sup>[18]</sup> During discharge, the reversed shift of the (003), (104) peak can be observed, indicating some opposite processes happens compared with charging. Notably, the changes of the peaks' position during the 2nd cycle are analogous to the first cycle, representing the parallel lithiation–delithiation mechanism, which coincides with the discussion above.

Recently, the observation of higher capacity in relevant systems tends to be ascribed to the oxygen-related anionic electrochemical process.<sup>[9,19,20]</sup> Thus, as a powerful tool to investigate the oxygen redox behaviors,<sup>[21,22]</sup> in situ Raman has been employed (Figure 3, wider Raman shift region is shown in Figure S6, Supporting Information). In order to collect shell-isolated nanoparticle-enhanced Raman signal, gold nanoparticles (NPs)  $\approx 40$  nm in diameter with an  $\text{SiO}_2$  coating shell ( $\approx 5$  nm) were synthesized as in previous reports.<sup>[23]</sup> The washed and dried  $\text{Au@SiO}_2$  NPs were dripped onto the specific cathode surface and vacuum dried before assembly. Regardless of the

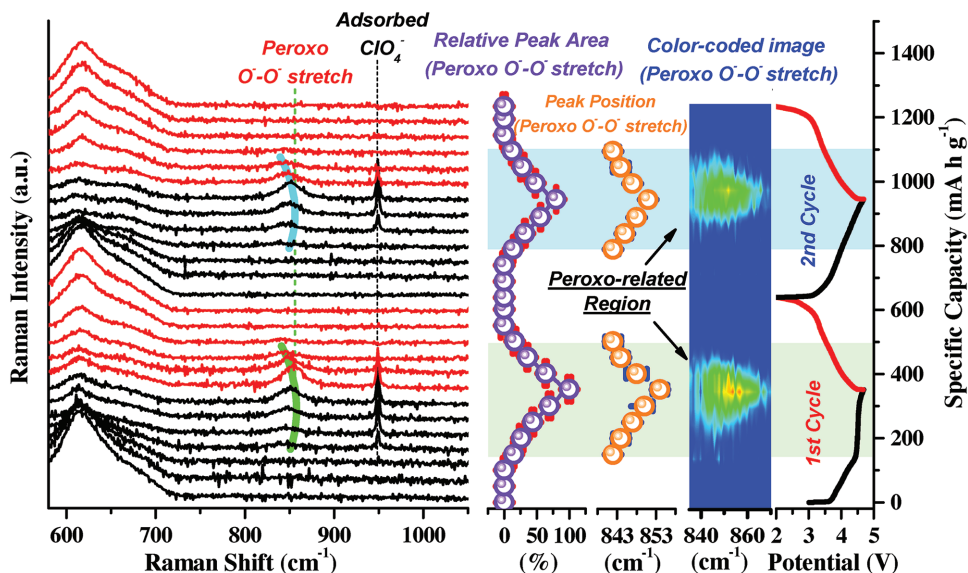


**Figure 3.** Capacity dependent in situ Raman spectra recorded during initial two galvanostatic cycles ( $5 \text{ mA g}^{-1}$ ). The novel peroxy-species peak has been highlighted, and corresponding capacity dependence of peak area (purple hollow), peak position (orange hollow), and color-coded image are summarized, respectively. The range of intensity distribution plots with reference color bar is from 0 to 0.03. The related voltage profiles are shown for clarity.

detailed analysis on overlapping stretching modes in  $\text{MO}_6$  octahedron (below  $700\text{ cm}^{-1}$ ),<sup>[24]</sup> the variation trend of several novel peaks become noteworthy during cycling. One sharp peak can be observed at  $953\text{ cm}^{-1}$  once the potential climbs up to 4.4 V, which is due to the adsorption of the anion in perchlorate salt ( $\text{ClO}_4^-$  symmetric stretching).<sup>[22]</sup> The related peak intensity quickly reaches maximum value due to the saturation of adsorption on the cathode surface. Besides, the unique adsorption feature can be further proved by the potential-dependent dropping trend during discharging (see more details in Figure S7, Supporting Information). More importantly, within the typical peroxy O—O stretch region ( $700\text{--}900\text{ cm}^{-1}$ ) in peroxy-species (see more details in Figure S8, Supporting Information),<sup>[9,22]</sup> a new peak at  $\approx 850\text{ cm}^{-1}$  emerges and increases during the 4.5 V related charging plateau, and gradually disappears with the subsequent discharge process. The potential of O—O peroxy bond appearance would be different in other systems resulting from different thermodynamic conditions, which means the environment (such as space group, neighbored atoms) surrounding oxygen atoms.<sup>[25]</sup> The reversible variation trend of the peroxy O—O bond can also be obtained on specific high voltage plateau during the 2nd cycle. The average concentration of peroxy O—O bond can be represented by relative peak area which is also shown in Figure 3. The relative peak area of peroxy O—O bond equals zero (means no O—O bond appears) before 4.5 V related charging plateau, then increases gradually to the maximum corresponding to the end of charging as a function of time. The area decreases to zero subsequently in discharge process and exhibits reversible variation trend during the 2nd cycle. Moreover, according to the obtained XRD results (Figure 2), the formation of the newly proposed peroxy O—O bond can be assigned to the delithiation from Li/TM layer. During charging at 4.5 V plateau, the shift of peroxy O—O stretch to higher wavenumber indicates the reduction of peroxy O—O bond length in peroxy-species.<sup>[18]</sup> The peroxy O—O bond length range can be empirically considered as 1.28–1.48 Å (1.28 Å in  $\text{Li}_2\text{O}_2$  where peroxy O—O bond located at  $790\text{ cm}^{-1}$  and 1.48 Å in  $\text{H}_2\text{O}_2$  where peroxy O—O bond located at  $878\text{ cm}^{-1}$ ).<sup>[26]</sup> Combining with the decreasing trend of *c*-axis length during related stage (Figure 2), the peroxy O—O bond tends to be formed along the *c*-axis (not in *ab* plane), which is also well consistent with the mechanism proposed by related density functional theory (DFT) simulations.<sup>[27]</sup> In this case, the causality among delithiation/lithiation between Li/TM layer, the variation of *c*-axis and the formation/decomposition of peroxy O—O bond can be rationally unified together. Consequently, essentially different from the peroxy-like ( $\text{O}_2$ )<sup>*n*-</sup>-based redox process proposed by previous ex situ X-ray photoelectron spectroscopy (XPS) analysis,<sup>[11,19,28]</sup> herein, the operando observation and assignment of real peroxy O—O bond in peroxy-species provides new evidence for the reversible anionic redox chemistry in Li-rich cathode materials. Furthermore, the similar phenomenon in  $\text{LiPF}_6$ -salt electrolyte (1 M in propylene carbonate) can be seen in Figure S9 in the Supporting Information. Moreover, XPS etching experiment reveals that the peroxy O—O bond exists both in the surface and in the bulk (see more details in Figure S10, Supporting Information).

Besides the typical irreversible oxygen loss (such as the formation of  $\text{O}_2$ ,  $\text{O}_2^-$ ) in the lithium rich materials,<sup>[9,29]</sup> herein, we demonstrate a reversible oxygen behavior with the generation of  $\text{O}_2^{2-}$  dimers, which can be sustainable in the subsequent cycle. To better understand the formation of the peroxy O—O bond during cycling, the first-principles calculations for the  $\text{Li}_{1.2-x}\text{Ni}_{0.2}\text{Mn}_{0.6}\text{O}_2$  systems have been performed. We note that the excess lithium ordering in the transition metal layer of  $\text{Li}_{1.2}\text{Ni}_{0.2}\text{Mn}_{0.6}\text{O}_2$  is very complicated and a mixture of different types of local ordering.<sup>[30]</sup> However, the  $\text{Li}_{1.2}\text{Ni}_{0.2}\text{Mn}_{0.6}\text{O}_2$  with honeycomb ordering of excess lithium atoms experiences an energy barrier of 1.4 eV for the formation of peroxy bonds, compared to 0.6–1 eV of  $\text{Li}_2\text{MnO}_3$ ,<sup>[31]</sup> which is not realistic to occur during the room temperature cycling (see Figures S11–S13, Supporting Information, for detailed discussions). Here, we are especially interested in  $\text{Li}_{1.2}\text{Ni}_{0.2}\text{Mn}_{0.6}\text{O}_2$  with local straight-type tripolymers (Figure S14, Supporting Information), where the formation of peroxy bonds experiences no energy barrier during charging.

Thus, the  $\text{Li}_{1.2}\text{Ni}_{0.2}\text{Mn}_{0.6}\text{O}_2$  crystal structure with local straight-type was built using a  $5 \times 2 \times 1$  supercell of the  $R\bar{3}m$   $\text{LiMnO}_2$  with partial Mn atoms replaced by Ni and Li atoms, as shown in Figure S14 in the Supporting Information. First, the  $\text{Li}_{1.2}\text{Ni}_{0.2}\text{Mn}_{0.6}\text{O}_2$  crystal structure was relaxed, and the optimized lattice parameters of  $\text{Li}_{1.2}\text{Ni}_{0.2}\text{Mn}_{0.6}\text{O}_2$  unit cell are  $a = 14.49$ ,  $b = 5.81$ , and  $c = 14.26$  Å, respectively. Then, the crystal structures and atomic positions of the  $\text{Li}_{1.2-x}\text{Ni}_{0.2}\text{Mn}_{0.6}\text{O}_2$  systems during the whole charging processes were relaxed, and the corresponding charge density distributions for  $x = 0.6, 0.7, 0.8, 0.9, 1.0$ , and  $1.1$  were shown in Figure 4. During the initial charging process ( $x$  from 0 to 0.6), some lithium atoms in lithium layers are preferentially divorced from the  $\text{Li}_{1.2-x}\text{Ni}_{0.2}\text{Mn}_{0.6}\text{O}_2$  cathode. No peroxy O—O bond is observed during this initial charging period. When reaching the middle period (i.e.,  $x = 0.7$ ), some excess lithium atoms in the TM-layers begin to leave from  $\text{Li}_{0.5}\text{Ni}_{0.2}\text{Mn}_{0.6}\text{O}_2$  cathode, and two adjacent O atoms of the  $\text{MnO}_6$  octahedron near the excess lithium vacancies get closer to each other. Moreover, remarkable electrons between these two closer O atoms can be observed (yellow isosurfaces in black dashed circles), demonstrating the formation of O—O covalent bond, and the corresponding O—O bond length is calculated to be 1.343 Å (Table 1), which is much shorter than 2.6 Å of interatomic distance between adjacent O atoms in  $\text{MnO}_6$  octahedrons, and even shorter than 1.49 Å of the peroxy O—O bond length in Li-Rich  $\text{Li}_2\text{MnO}_3$  system.<sup>[31]</sup> According to the Bader charge data (Figure S15, Supporting Information), the O atomic charges of the special O—O bond in  $\text{Li}_{0.5}\text{Ni}_{0.2}\text{Mn}_{0.6}\text{O}_2$  cathode are larger than those in  $\text{Li}_{0.6}\text{Ni}_{0.2}\text{Mn}_{0.6}\text{O}_2$  and other O atoms far from the excess lithium vacancies. All these evidence indicate the formation of the peroxy O—O bond between  $x = 0.6$  and 0.7, corresponding to the specific capacity between 190 and 220 mA h  $\text{g}^{-1}$ , which is consistent with the in situ Raman spectra data. During the final charging period ( $x = 0.8\text{--}1.1$ ), more and more peroxy O—O bonds form with smaller bond lengths and more positive O atomic charges, which is also consistent with the variation trend of Raman shift and relative peak area of O—O bonds in our in situ Raman spectra data.

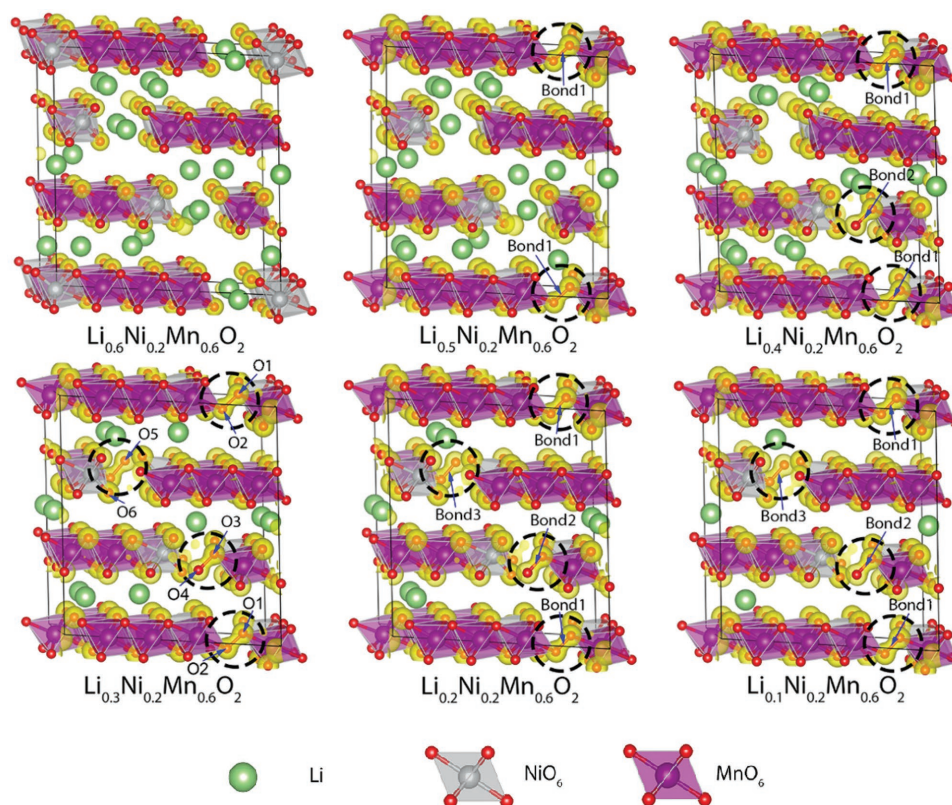


**Figure 4.** Charge density distributions (yellow isosurfaces =  $0.2 \text{ e} \text{ \AA}^{-3}$ ) of the  $\text{Li}_{1.2-x}\text{Ni}_{0.2}\text{Mn}_{0.6}\text{O}_2$  systems ( $x = 0.6, 0.7, 0.8, 0.9, 1.0,$  and  $1.1$ ) with peroxo O—O bonds (in the black dashed circles) during the charging and discharging processes.

The processes summarizing the aforementioned discussion are as follows: At first,  $\text{Li}^+$  migrates out from Li layers with the charge compensation by  $\text{Ni}^{2+/4+}$  redox couple, corresponding to  $\approx 130 \text{ mA h g}^{-1}$ . From then on, oxidation of oxygen starts to emerge for charging compensation till the end of the charging because  $\text{Ni}^{2+}$  is totally oxidized to  $\text{Ni}^{4+}$  and  $\text{Mn}^{4+}$  cannot be oxidized to a higher valence state in octahedral site.<sup>[32]</sup> Afterward, the oxidation of oxygen is the main responsible for charge compensation at the plateau of  $\approx 4.5 \text{ V}$ . Since about 1.1  $\text{Li}^+$  can be extracted from the structure,  $\text{Li}^+$  continues to be removed out from Li layers and TM layers accompanied with appearance of peroxo O—O bond. The cooperative effect of anionic redox and extraction of  $\text{Li}^+$  leads to the smooth change of  $c$ -lattice parameter and eventually turns it back to a lower value at this process. Figure S16 in the Supporting Information shows the par-

**Table 1.** The peroxo O—O bond length (in  $\text{\AA}$ ) of the  $\text{Li}_{1.2-x}\text{Ni}_{0.2}\text{Mn}_{0.6}\text{O}_2$  systems ( $x = 0.6, 0.7, 0.8, 0.9, 1.0,$  and  $1.1$ ) during the charging and discharging processes.

	O—O bond1	O—O bond2	O—O bond3
$\text{Li}_{0.6}\text{Ni}_{0.2}\text{Mn}_{0.6}\text{O}_2$	—	—	—
$\text{Li}_{0.5}\text{Ni}_{0.2}\text{Mn}_{0.6}\text{O}_2$	1.343	—	—
$\text{Li}_{0.4}\text{Ni}_{0.2}\text{Mn}_{0.6}\text{O}_2$	1.315	1.415	—
$\text{Li}_{0.3}\text{Ni}_{0.2}\text{Mn}_{0.6}\text{O}_2$	1.314	1.348	1.350
$\text{Li}_{0.2}\text{Ni}_{0.2}\text{Mn}_{0.6}\text{O}_2$	1.306	1.308	1.341
$\text{Li}_{0.1}\text{Ni}_{0.2}\text{Mn}_{0.6}\text{O}_2$	1.305	1.307	1.310

ticipation of  $\text{Ni}^{2+}$  and oxygen involvement during the charging process. The charge compensation during discharging process is similar with charging process. The changes of  $c$ -lattice parameter shows a cooperation including the reversible anionic ( $\text{O}^-/\text{O}^{2-}$ ) redox process, the reduction of Ni and the reinsertion of  $\text{Li}^+$  into the structure. Moreover, combining the changes of peroxo O—O bond length in Raman results with the variation tendency of  $c$ -axis length in XRD results, the formation of peroxo O—O bond is speculated along the  $c$ -axis, which is also confirmed by the DFT calculations.

In summary, the typical Li-rich positive material  $\text{Li}_{1.2}\text{Ni}_{0.2}\text{Mn}_{0.6}\text{O}_2$  was systematically studied. Based on the advanced in situ technologies, we can directly visualize the structural evolution accompanied by the (de)lithiation, including the reversible anionic redox process, even peroxo O—O bond formation and extinction along  $c$  axis, which are consistent well with the DFT calculations. What is more, both cationic and anionic redox processes are reversible even in subsequent cycles, enabling Li-rich layered oxides a high capacity. Our findings highlight a new evidence for the reversible anionic redox process in Li-rich cathode materials and provide a deep understanding of intercalation chemistry and new insights into the design of high-performance Li-rich layered oxides.

## Supporting Information

Supporting Information is available from the Wiley Online Library or from the author.

## Acknowledgements

X.L. and Y.Q. contributed equally to this work. X.L. is grateful for financial support of the CSC (China Scholarship Council) scholarship. This work was partially supported financially by National Basic Research Program of China (2014CB932302 and 2014CB932303), Natural Science Foundation of Jiangsu Province of China (BK20170630), the Fundamental Research Funds for the Central Universities (021314380076 and 021314380080), the National Natural Science Foundation of China (21673116, 2163303, 51602144), and the Natural Science Foundation of Jiangsu Province of China (BK20160068). The authors are very grateful to Prof. Ying Shirley Meng and Prof. Shou-Hang Bo for the discussion.

## Conflict of Interest

The authors declare no conflict of interest.

## Keywords

in situ Raman spectroscopy, in situ X-ray diffraction, Li-ion batteries, Li-rich materials, oxygen redox

Received: September 11, 2017

Revised: January 5, 2018

Published online: February 19, 2018

- [1] a) J. B. Goodenough, Y. Kim, *Chem. Mater.* **2010**, *22*, 587; b) M. S. Whittingham, *Chem. Rev.* **2004**, *104*, 4271; c) A. S. Arico, P. Bruce, B. Scrosati, J. M. Tarascon, W. Van Schalkwijk, *Nat. Mater.* **2005**, *4*, 366; d) J. M. Tarascon, M. Armand, *Nature* **2001**, *414*, 359; e) P. He, H. J. Yu, D. Li, H. S. Zhou, *J. Mater. Chem.* **2012**, *22*, 3680.
- [2] a) Z. D. Huang, X. M. Liu, B. A. Zhang, S. W. Oh, P. C. Ma, J. K. Kim, *Scr. Mater.* **2011**, *64*, 122; b) Y. Jiang, H. Zhuang, Q. L. Ma, Z. Jiao, H. J. Zhang, R. Z. Liu, Y. L. Chu, B. Zhao, *J. Mater. Res.* **2013**, *28*, 1505; c) S. Y. Yang, X. Y. Wang, X. K. Yang, L. Liu, Z. L. Liu, Y. S. Bai, Y. P. Wang, *J. Solid State Electrochem.* **2012**, *16*, 1229; d) L. J. Xi, C. W. Cao, R. G. Ma, Y. Wang, S. L. Yang, J. Q. Deng, M. Gao, F. Lian, Z. G. Lu, C. Y. Chung, *Phys. Chem. Chem. Phys.* **2013**, *15*, 16579.
- [3] J. S. Kim, C. S. Johnson, J. T. Vaughey, M. M. Thackeray, S. A. Hackney, *Chem. Mater.* **2004**, *16*, 1996.
- [4] D. L. Ye, G. Zeng, K. Nogita, K. Ozawa, M. Hankel, D. J. Searles, L. Z. Wang, *Adv. Funct. Mater.* **2015**, *25*, 7488.
- [5] Y. D. Wang, J. W. Jiang, J. R. Dahn, *Electrochem. Commun.* **2007**, *9*, 2534.
- [6] H. J. Yu, Y. G. So, A. Kuwabara, E. Tohigi, N. Shibata, T. Kudo, H. S. Zhou, Y. Ikuhara, *Nano Lett.* **2016**, *16*, 2907.
- [7] a) M. M. Thackeray, C. S. Johnson, J. T. Vaughey, N. Li, S. A. Hackney, *J. Mater. Chem.* **2005**, *15*, 2257; b) Z. H. Lu, D. D. MacNeil, J. R. Dahn, *Electrochem. Solid-State Lett.* **2001**, *4*, A191.
- [8] C. S. Johnson, J. S. Kim, C. Lefief, N. Li, J. T. Vaughey, M. M. Thackeray, *Electrochem. Commun.* **2004**, *6*, 1085.
- [9] K. Luo, M. R. Roberts, R. Hao, N. Guerrini, D. M. Pickup, Y. S. Liu, K. Edstrom, J. H. Guo, A. V. Chadwick, L. C. Duda, P. G. Bruce, *Nat. Chem.* **2016**, *8*, 684.
- [10] D. H. Seo, J. Lee, A. Urban, R. Malik, S. Kang, G. Ceder, *Nat. Chem.* **2016**, *8*, 692.
- [11] M. Sathiy, G. Rousse, K. Ramesha, C. P. Laisa, H. Vezin, M. T. Sougrati, M. L. Doublet, D. Foix, D. Gonbeau, W. Walker, A. S. Prakash, M. Ben Hassine, L. Dupont, J. M. Tarascon, *Nat. Mater.* **2013**, *12*, 827.
- [12] E. McCalla, A. M. Abakumov, M. Saubanere, D. Foix, E. J. Berg, G. Rousse, M. L. Doublet, D. Gonbeau, P. Novak, G. Van Tendeloo, R. Dominko, J. M. Tarascon, *Science* **2015**, *350*, 1516.
- [13] K. A. Jarvis, Z. Q. Deng, L. F. Allard, A. Manthiram, P. J. Ferreira, *Chem. Mater.* **2011**, *23*, 3614.
- [14] a) A. C. Larson, R. B. Von Dreele, *Los Alamos Natl. Lab. Rep.* **1994**, 86; b) B. H. Toby, *J. Appl. Crystallogr.* **2001**, *34*, 210.
- [15] Z. H. Lu, J. R. Dahn, *J. Electrochem. Soc.* **2002**, *149*, A1454.
- [16] a) L. Zhang, H. Noguchi, *J. Electrochem. Soc.* **2003**, *150*, A601; b) Z. H. Lu, L. Y. Beaulieu, R. A. Donabarger, C. L. Thomas, J. R. Dahn, *J. Electrochem. Soc.* **2002**, *149*, A778.
- [17] D. Mohanty, S. Kalnaus, R. A. Meisner, K. J. Rhodes, J. L. Li, E. A. Payzant, D. L. Wood, C. Daniel, *J. Power Sources* **2013**, *229*, 239.
- [18] J. M. Tarascon, G. Vaughan, Y. Chabre, L. Seguin, M. Anne, P. Strobel, G. Amatucci, *J. Solid State Chem.* **1999**, *147*, 410.
- [19] P. E. Pearce, A. J. Perez, G. Rousse, M. Saubanere, D. Batuk, D. Foix, E. McCalla, A. M. Abakumov, G. Van Tendeloo, M. L. Doublet, J. M. Tarascon, *Nat. Mater.* **2017**, *16*, 850.
- [20] B. Qiu, M. H. Zhang, Y. G. Xia, Z. P. Liu, Y. S. Meng, *Chem. Mater.* **2017**, *29*, 908.
- [21] Y. Qiao, S. Wu, J. Yi, Y. Sun, S. Guo, S. Yang, P. He, H. Zhou, *Angew. Chem., Int. Ed.* **2017**, *56*, 4960.
- [22] Y. Qiao, S. Ye, *J. Phys. Chem. C* **2015**, *119*, 12236.
- [23] J. F. Li, Y. F. Huang, Y. Ding, Z. L. Yang, S. B. Li, X. S. Zhou, F. R. Fan, W. Zhang, Z. Y. Zhou, D. Y. Wu, B. Ren, Z. L. Wang, Z. Q. Tian, *Nature* **2010**, *464*, 392.
- [24] P. Lanz, C. Villevieille, P. Novak, *Electrochim. Acta* **2014**, *130*, 206.
- [25] a) M. Sathiy, A. M. Abakumov, D. Foix, G. Rousse, K. Ramesha, M. Saubanere, M. L. Doublet, H. Vezin, C. P. Laisa, A. S. Prakash, D. Gonbeau, G. VanTendeloo, J. M. Tarascon, *Nat. Mater.* **2015**, *14*, 230; b) T. Ohzuku, A. Ueda, M. Nagayama, *J. Electrochem. Soc.* **1993**, *140*, 1862; c) S. H. Park, S. W. Oh, S. H. Kang, I. Belharouak, K. Amine, Y. K. Sun, *Electrochim. Acta* **2007**, *52*, 7226; d) N. Yabuuchi, K. Kubota, M. Dahbi, S. Komaba, *Chem. Rev.* **2014**, *114*, 11636; e) M. Guignard, C. Didier, J. Darriet, P. Bordet, E. Elkaïm, C. Delmas, *Nat. Mater.* **2013**, *12*, 74.
- [26] a) A. J. Bridgeman, J. Rothery, *J. Chem. Soc. Dalton Trans.* **1999**, 4077; b) Z. X. Liu, L. R. De Jesus, S. Banerjee, P. P. Mukherjee, *ACS Appl. Mater. Interfaces* **2016**, *8*, 23028.
- [27] M. Saubanere, E. McCalla, J. M. Tarascon, M. L. Doublet, *Energy Environ. Sci.* **2016**, *9*, 984.
- [28] D. Foix, M. Sathiy, E. McCalla, J. M. Tarascon, D. Gonbeau, *J. Phys. Chem. C* **2016**, *120*, 862.
- [29] a) A. R. Armstrong, M. Holzapfel, P. Novak, C. S. Johnson, S. H. Kang, M. M. Thackeray, P. G. Bruce, *J. Am. Chem. Soc.* **2006**, *128*, 8694; b) S. Hy, F. Felix, J. Rick, W. N. Su, B. J. Hwang, *J. Am. Chem. Soc.* **2014**, *136*, 999.
- [30] a) K. Luo, M. R. Roberts, N. Guerrini, N. Tapia-Ruiz, R. Hao, F. Massel, D. M. Pickup, S. Ramos, Y. S. Liu, J. Guo, *J. Am. Chem. Soc.* **2016**, *138*, 11211; b) M. Gu, I. Belharouak, A. Genc, Z. Wang, D. Wang, K. Amine, F. Gao, G. Zhou, S. Thevuthasan, D. R. Baer, *Nano Lett.* **2012**, *12*, 5186; c) M. M. Thackeray, S. H. Kang, C. S. Johnson, J. T. Vaughey, R. Benedek, S. Hackney, *J. Mater. Chem.* **2007**, *17*, 3112.
- [31] H. R. Chen, M. S. Islam, *Chem. Mater.* **2016**, *28*, 6656.
- [32] J. Roos, C. Eames, S. M. Wood, A. Whiteside, M. S. Islam, *Phys. Chem. Chem. Phys.* **2015**, *17*, 22259.